Nanoscale Horizons

ROYAL SOCIETY OF CHEMISTRY

COMMUNICATION

View Article Online
View Journal | View Issue

Cite this: *Nanoscale Horiz.*, 2025, 10, 2504

Received 4th June 2025,
Accepted 22nd July 2025

DOI: 10.1039/d5nh00395d

rsc.li/nanoscale-horizons

Photophysical structured illumination velocimetry based on the long-lasting emission response of lanthanide luminescent nanoparticles†

Haichun Liu * and Jerker Widengren *

This study introduces the concept of photophysical structured illumination velocimetry (PP-SIV), verified through comprehensive numerical simulations. PP-SIV can capture two-dimensional (2D) flow velocity fields from a single snapshot image of the emission pattern from luminescent probes, leveraging the suitable photodynamics of the probes and using the applied excitation field pattern as reference. By eliminating the need for any beam or sample scan, PP-SIV has the potential to significantly accelerate the data acquisition process required for velocity field imaging. Furthermore, with excitation patterns applied at different depths, three-dimensional (3D) flow imaging can be potentially achieved. We propose lanthanide-based upconversion nanoparticles (UCNPs), particularly those capable of both absorbing and emitting within the highly biocompatible and transparent NIR-II window (1000–1700 nm), as promising probe candidates for implementing PP-SIV. This concept holds significant potential to pave the way for rapid, three-dimensional (3D) blood flow imaging at sufficient speeds for real-time monitoring of hemodynamic events in the brain.

New concepts

We establish and validate a new concept—photophysical structured illumination velocimetry (PP-SIV)—through comprehensive numerical simulations, aiming to address a key challenge in volumetric vasculature imaging in the brain: resolving blood flow dynamics at greater depths. By implementing PP-SIV, a two-dimensional flow velocity field can be extracted from a single emission pattern measurement of the probes, using the structured illumination pattern as reference. The PP-SIV approach is clearly distinct from previously established methods that rely on the micro-scale positioning and tracking of individual particles (or red blood cells) to assess their local displacements to reconstruct flow velocity fields, such as micro-particle image velocimetry, micro-particle tracking velocimetry, and two-photon laser scanning microscopy. PP-SIV eliminates the need for source scans, which currently impose a major limitation on the imaging speed of state-of-the-art blood flow imaging techniques, potentially enabling three-dimensional flow imaging with sufficient speed for real-time monitoring of most hemodynamic events. We propose lanthanide-based upconversion nanoparticles as promising probe candidates for implementing PP-SIV, particularly those capable of both absorbing and emitting within the highly biocompatible and transparent second near-infrared window (1000–1700 nm). Our study demonstrates the potential of PP-SIV for flow imaging and provides a solid foundation for future experimental validations.

1. Introduction

In vivo cerebral imaging of vasculature and hemodynamics in three-dimensional (3D) volumes is vital for brain research. At spatial scales of vascular function and regulation, several rigorous methods can be used to study blood flow, including laser Doppler velocimetry,[1] blood-oxygenation level-dependent functional magnetic resonance imaging (BOLD fMRI),[2] and two-photon laser scanning microscopy (TPLSM).[3–6] However, they are all inevitably constrained by slow imaging speeds and/or limited imaging depths. Currently, volumetric vasculature imaging in the brain, at speeds resolving blood flows, at larger depths and with sub-capillary spatial resolution remains an extremely challenging task.

The fundamental reason behind the sluggish imaging pace of these techniques stems from the mandatory scanning of the source. For example, in TPLSM for blood flow imaging velocity data is extracted by tracking the movements of fluorophore-labeled red blood cells between successive line image captures, a process heavily dependent on rapid laser scanning. To capture hemodynamic events (typically on μs-to-s timescales), TPLSM is most often used to record one-dimensional (1D) line scans (usually at hundreds to thousands of lines per second) to create two-dimensional (2D) frames.[7] 3D monitoring of blood flow adds further constraints, requiring sequential scanning of the excitation focus in multiple planes along the axial direction. Altogether, this makes standard TPLSM with a Gaussian laser beam inadequate for real-time monitoring of most hemodynamic events. Only by adopting an axially elongated Bessel beam, which when scanned in two dimensions transforms the

Department of Applied Physics, KTH Royal Institute of Technology, S-106 91 Stockholm, Sweden.
E-mail: haichun@kth.se, jwideng@kth.se

† Electronic supplementary information (ESI) available. See DOI: https://doi.org/10.1039/d5nh00395d

2D frame rate into a 3D rate, a solution emerges for quasi-3D blood flow imaging.[7] The inertia of scanning components imposes restrictions that cap the 2D imaging frame rate at a maximum of tens of frames per second (fps), rendering the 3D imaging volume rate unacceptably slow to monitor most hemodynamic events.

Here, to bypass the reliance on source scans and their limitations in imaging speed, a concept is proposed, based on patternization of the flow-velocity field, as a basis for a scan-free, rapid volumetric flow imaging technique. The concept, based on structured illumination and leveraging the suitable photophysics of the probes, we name photophysical structured illumination velocimetry (PP-SIV). Herein, a photoluminescence pattern is captured and then compared with the structured illumination pattern used to generate it. The relative spatial shift between these two patterns then provides a quantity from which the flow velocity field can be extracted, thereby enabling rapid mapping of a flow-velocity field from a single snapshot image. While it has long been recognized that extended luminescence lifetimes of luminophores pose a significant challenge for fast optical imaging, it is precisely this characteristic that serves as the enabling cornerstone in the rapid volumetric flow imaging method proposed in this work. PP-SIV leverages the long-lasting luminescence of the probes and can analyze the collective emission patterns formed by all probes within the field of view. This makes PP-SIV a holistic flow imaging technique, fundamentally different from microscale positioning-based flow velocimetry methods such as particle image velocimetry (PIV) and particle tracking velocimetry (PTV),[8] which rely on transient luminescent or scattered signals and require tracking of individual particles to reconstruct flow fields.

In this study, the feasibility of the PP-SIV concept was investigated through comprehensive numerical simulations. Initially, the photoluminescence kinetics of potential luminophores for PP-SIV was modelled, using Er–Ho-codoped lanthanide luminescent nanoparticles (LNPs) with upconverted emission[9] as a representative example, and their response to modulated excitation light was then analyzed. Subsequently, the photoluminescence pattern of the LNPs, generated by a periodic excitation pattern upon motion of the LNPs in a flowing medium under different velocities, was simulated, analyzing also the degree of spatial shift of the photoluminescence pattern relative to the excitation pattern. Replicating typical cerebral vascular conditions, with flow velocities ranging from 1 to 10 mm s^{-1}, and employing an appropriate spatial periodicity for the excitation pattern, our analyses showed that distinct spatial shifts can then be obtained, enabling the retrieval of flow velocity information. Furthermore, utilizing the calculated emission-pattern data, the inverse problem was tackled, demonstrating how various algorithms could be used to reconstruct the flow velocity field from the spatial shifts in luminescence images, thus validating the efficacy of the PP-SIV concept. Beyond examining the simplest flow scenario—a straight vessel with spatially constant velocity—the feasibility of PP-SIV was explored under more complex flow conditions involving spatially continuous variations in both flow direction (within a 2D plane) and velocity, where our findings confirmed the validity of the PP-SIV concept under more diverse conditions.

2. Results

2.1 Photophysical structured illumination velocimetry (PP-SIV)

The foundation of the PP-SIV concept lies in the frequency-domain (FD) response of luminophores. The photoluminescence process of LNPs typically entails multiple energy states and transitions, including both light-driven and spontaneous processes, as well as potential interactions among different optical centers constituting the luminophores. As an example, a two-photon upconversion nanoparticle (UCNP) (Fig. 1a) was considered, where the sensitizer ion undergoes two absorption steps—ground-state absorption (GSA) and excited-state absorption (ESA)—to populate the excited state of the activator ion and produce upconverted emission. Under sinusoidally modulated excitation in the time domain, the emission of the luminophores would exhibit a phase lag relative to the excitation intensity (Fig. 1b), a phenomenon dependent on both the modulation frequency (f) and the intrinsic photophysical parameters of the luminophores.

Within the fluorescence community, this temporal frequency-domain (TFD) response of luminophores offers a method to quantify fluorescence lifetimes.[10] In PP-SIV the opposite approach is instead applied, taking the luminescence lifetime and photodynamics of the LNPs as known parameters, and then using the TFD response to determine the flow of the LNPs, where the flow affects the excitation modulation applied onto the LNPs, and thereby also their TFD response. A similar inverse strategy has been proposed in a confocal microscopy setting, for point-wise diffusion measurements of fluorescent molecules on sub-micrometer scales.[11] Therein, a variable buildup of photoinduced reversible dark states in fluorescent molecules, depending on their passage times, was reflected in the time-averaged fluorescence intensity, enabling mobility characterization.[11] However, the transient dark (photo-isomerized) states of the fluorophores used in the latter readout typically themselves depend on the local environment. Similarly, for the PP-SIV approach to be useful on a larger scale, the luminescence lifetimes and photodynamics of the luminophores to be used must be "inert", *i.e.* not change with the local environmental conditions in the flow to be imaged. Indeed, LNPs can be constructed with the lanthanide ions well protected in the matrix material of the LNPs, thereby fulfilling this requirement. Second, PP-SIV also specifically takes advantage of the longer luminescence lifetimes of LNPs.

For fluorophores, which typically display rapid fluorescence kinetics with lifetimes ranging from 0.1 to 10 ns, a phase lag of 0 to 90° is observed under modulation frequencies of 1–1000 MHz.[10] In contrast, LNPs, particularly UCNPs, with longer-lived energy states lasting up to a few milliseconds, and involving multiple transition and interaction steps, may exhibit more pronounced phase lags, reaching up to 180°, and under much lower modulation frequencies, typically below 100 kHz.[12,13] As discussed in the following analysis, the ability of LNPs to

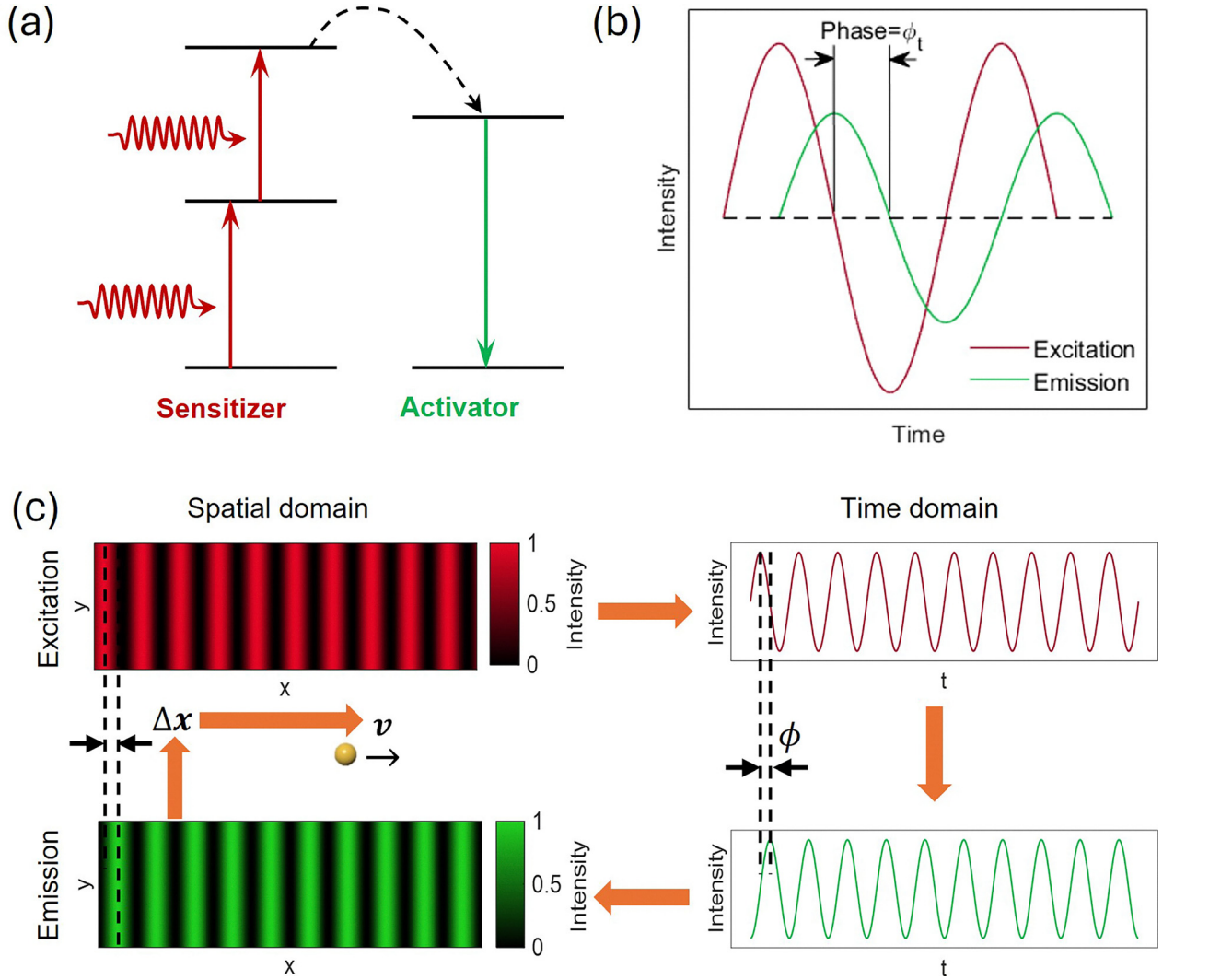

Fig. 1 Principle of photophysical structured illumination velocimetry (PP-SIV): (a) Simplified energy level diagram depicting a two-photon upconversion luminescence process. (b) Response of upconversion luminescence to a sinusoidally modulated excitation intensity. (c) Imaging principle in PP-SIV, here illustrated by UCNPs moving along the x-direction with a constant velocity v, through a spatially structured illumination pattern with a spatial period Λ. Due to the motion of the nanoparticles, they experience a periodic excitation-intensity function in the time domain, with a modulation frequency $f = \frac{v}{\Lambda}$. The emission intensity of the UCNPs exhibits a phase lag ϕ relative to the excitation intensity, dependent on the modulation frequency f and thereby also on the velocity of the UCNPs v. The phase lag in the time domain would be projected as a shift Δx in the emission pattern relative to the excitation pattern. By analyzing the spatial shift Δx, the nanoparticle velocity v can be extracted. Orange arrows indicate the workflow of the PP-SIV concept.

generate significant phase lags at low modulation frequencies is a key advantage—and indeed the enabling property—for implementing the PP-SIV approach. This characteristic allows for the measurement of cerebral hemodynamic-relevant blood flow velocities using excitation patterns with reasonable spatial periods.

Consider a luminophore, such as a UCNP, moving along the x-direction at a constant velocity v, passing through a spatially structured illumination pattern with a spatial period Λ (Fig. 1c). It then experiences a periodic excitation intensity $I_{exc}(t)$ in the time domain, with a modulation frequency:

$$f = \frac{v}{\Lambda}. \quad (1)$$

Following complex multi-step excitations of the UCNPs, the resulting emission intensity in the time domain, $I_{em}(t)$, exhibits a similar periodicity to the excitation function but displays a phase lag ϕ. This phase lag depends on the modulation frequency f and consequently, the velocity v of the luminophore, as per eqn (1). This phase lag in the time domain, when projected onto the spatial domain, translates into a shift Δx in the emission pattern relative to the excitation pattern, given by:

$$\Delta x = \frac{\phi(f)}{360} \cdot \Lambda = \frac{\phi(v)}{360} \cdot \Lambda. \quad (2)$$

By analyzing this spatial shift Δx, given the dependence of ϕ on the luminophore velocity v, we can extract v.

A crucial aspect to consider is how large the spatial shift in the emission pattern is relative to the excitation pattern and whether it is discernible by a camera within a microscopic imaging setup. Most organic fluorophores have fluorescence

lifetimes in the nanosecond time range, and noticeable phase lags are then only attainable at modulation frequencies of MHz and above. Given a spatial period $\Lambda = 2$ μm for the illumination pattern and a typical flow velocity range within cerebral vasculature of 1–10 mm s^{-1},[4] the equivalent modulation frequency experienced by the luminophores as they flow across this pattern is then between 0.5 and 5 kHz as per eqn (1). This range may be too low to yield any noticeable phase lag ϕ in the emission from organic fluorophores. Consequently, it would be very challenging, if at all possible, to distinguish the spatial projection of this phase lag, *i.e.*, the emission pattern shift Δx, using a camera within a microscope setup.

It can be argued that successful implementation of PP-SIV for hemodynamic studies relies on luminophores with slow luminescent kinetics, such that substantial shifts in their emission pattern are generated when they are moving across structured illumination patterns at relevant velocities. In this context, LNPs, and particularly UCNPs feature multiple long-lived excited states and multi-step population processes, resulting in significantly slower photoluminescence kinetics than in organic fluorophores. Moreover, their photophysical properties can be fine-tuned through nanoparticle engineering.

In this regard, we investigated the suitability of UCNPs as reporters for PP-SIV through comprehensive numerical simulations, based on previously reported photophysical parameter values for potential UCNPs.

2.2 Potential UCNPs for PP-SIV and their temporal frequency-domain (TFD) responses

A critical factor in selecting PP-SIV probes is the operational spectral range. Recently, near-infrared (NIR)-emissive fluorescent probes operating within the NIR-II window (1000–1700 nm) have attracted considerable interest in *in vivo* fluorescence imaging, largely due to significantly reduced light scattering and diminished autofluorescence. However, practical NIR-II emissive probes remain scarce. Among reported NIR-II probes, including organic fluorophores,[14] carbon nanotubes,[15] and quantum dots,[16,17] LNPs show substantial promise, benefiting from abundant NIR-II emission channels, high brightness, and excellent biocompatibility.[18–21] These benefits and the utility of LNPs in preclinical NIR-II imaging have been demonstrated in several recent studies, for dynamic imaging of cancer immunotherapy in mice,[19] *in vivo* tracking of cancer vaccines and the elicited immune responses,[20] oxyhemoglobin saturation imaging,[22] and *in vivo* imaging of blood vasculature in the mouse brain.[18]

Among LNPs, NIR-II UCNPs offer distinct advantages for cerebral blood flow imaging, thanks to the significant penetration depths in biological tissues of both the applied excitation and the resulting emission light, and due to the nonlinear response of UCNPs to excitation intensity. Moreover, the diverse energy states within the lanthanide element group provide ample opportunities for designing tailored UCNPs. In this study, we focus specifically on Er–Ho-codoped UCNPs. Previous studies have demonstrated the efficacy of Er–Ho-codoped UCNPs (*e.g.*, $NaErF_4$:2%Ho@$NaYF_4$ core–shell UCNPs) in response to ~1500 nm light excitation, resulting in Ho^{3+} emission at approximately 1180 nm through a two-photon upconversion process,[9] with relatively low attenuation of both excitation and emission light within biological tissues. Through comprehensive numerical simulations, we explored the further suitability of these UCNPs in PP-SIV.

The simplified NIR-II UCL process of Er–Ho-codoped UCNPs under ~1500 nm light excitation is illustrated in Fig. 2a (more processes could be involved, as illustrated in Fig. S1, ESI†). Initially, the Er^{3+} $^4I_{11/2}$ excited state is efficiently populated by ~1500 nm light *via* a two-step process involving ground state absorption (GSA, populating the $^4I_{13/2}$ excited state) and excited state absorption (ESA, populating the $^4I_{9/2}$ excited state) followed by multi-phonon assisted non-radiative decay ($^4I_{9/2} \rightarrow {}^4I_{11/2}$).[9] Subsequently, an energy transfer (ET) process excites the Ho^{3+} $^5I_6$ state, leading to the generation of ~1180 nm emission.[9] Based on the more detailed model in Fig. S1 (ESI†) and using a rate equation approach (Section S1, ESI†), numerical simulations were exployed to explore the TFD response of Er–Ho-codoped UCNPs to a sinusoidally modulated excitation. The photophysical parameters used in the simulations are summarized in Table S1 (ESI†) and were primarily adopted or adapted from our previous work.[23] In particular, the excited-state lifetimes of Er^{3+} and Ho^{3+} were taken or adapted from this source. Energy transfer and cross-relaxation coefficients were also estimated based on ref. 23, remaining within a physically reasonable range.

The phase lag of the 1180 nm UCL emitted by Ho^{3+} ions was first simulated in response to a sinusoidally modulated excitation intensity, modeled as:

$$I_{exc}(t) = I_{avg}[1 + M_{exc}\sin(2\pi ft)], \quad (3)$$

where I_{avg} is average excitation intensity, and M_{exc} is the modulation depth. After an initial stabilization period, the UCL mirrors the sinusoidal excitation but with a phase lag relative to the excitation function, as shown in Fig. S2 (ESI†). By fitting the stabilized UCL waveform to a sinusoidal function, with the same frequency as the excitation and with the phase lag ϕ as one of the fitted parameters (together with the average intensity I_{UCL} and the modulation degree M_{UCL} for the UCL), *i.e.*,

$$I_{UCL}(t) = I_{UCL}[1 + M_{UCL}\sin(2\pi ft + \phi)], \quad (4)$$

we extracted the phase lag ϕ of the UCL.

It was then simulated how this phase lag varies with different modulation frequencies, while keeping the average excitation intensity (100 W cm^{-2}) and modulation depth ($M_{exc} = 1.0$) constant. As illustrated in Fig. 2b, the UCL demonstrates a notable phase lag in relation to the excitation intensity waveform, steadily increasing with modulation frequency. Notably, this phase lag becomes prominent even at relatively low frequencies, below 1 kHz, considerably lower than the typical modulation frequencies required to observe phase lags in the emission from organic fluorophores. This is attributed to the long excited-state lifetimes of the lanthanide ions involved, reaching up to a few milliseconds. At a modulation frequency of $f = 500$ Hz, ϕ reaches approximately 87°, close to the maximum ϕ found in

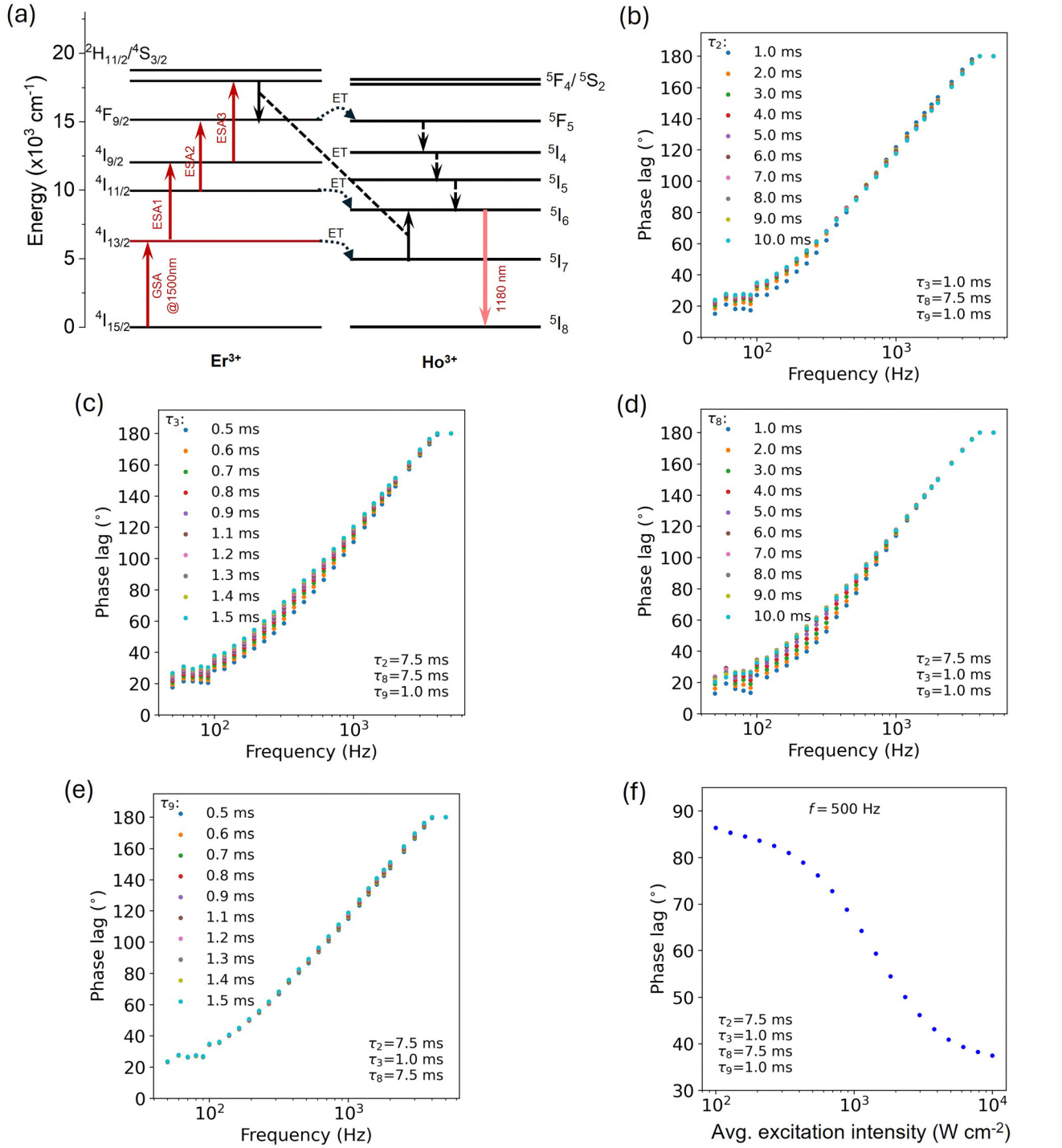

Fig. 2 (a) Simplified energy transfer mechanism in Er–Ho-codoped NIR-II UCNPs. GSA-ground state absorption; ESA-excited state absorption; ET-energy transfer. (b)–(e) Phase lag of the 1180 nm UCL emitted by Ho^{3+} ions in response to a sinusoidally modulated excitation intensity applied at different modulation frequencies with a fixed modulation amplitude (100 W cm^{-2}) and modulation degree (M_{exc} = 1.0). Effect of (b) the lifetime of the Er^{3+} $^4I_{13/2}$ state, τ_2, (c) the lifetime of the Er^{3+} $^4I_{11/2}$ state, τ_3, (d) the lifetime of the Ho^{3+} $^5I_7$ state, τ_8, and (e) the lifetime of the Ho^{3+} $^5I_6$ state, τ_9. (f) The influence of excitation intensity on the acquired phase lag of the 1180 nm UCL.

conventional fluorophores (at $f \gg$ MHz).[10] Then, for $f >$ 500 Hz, and in contrast to conventional Stokes-shifted fluorescence, the phase lag, ϕ, of this UCL can even surpass 90° and approach 180°, a characteristic also observed in our prior investigations of NIR-I- and visible-emitting UCNPs.[12,13] The saturation in the phase lag of UCL is a typical phenomenon in FD lifetime measurements, occurring at modulation frequencies high enough that the fluorophore can no longer follow the modulation.[10]

The phase lag of the UCL is primarily determined by the photophysical parameters inherent to the system.

Subsequently, the impact of the lifetimes associated with crucial energy states was investigated, the $^4I_{13/2}$ and $^4I_{11/2}$ states of Er^{3+} and the $^5I_7$ and $^5I_6$ states of Ho^{3+}. The findings indicate that the phase lag is substantially influenced by τ_2, τ_3, and τ_8, particularly at modulation frequencies below 1 kHz, while τ_9 shows negligible effect in the investigated ranges, as depicted in Fig. 2b–e. These dependencies offer avenues for customizing the phase lag through nanoparticle engineering by adjusting doping concentrations, in view of that the apparent lifetimes of lanthanide excited states heavily rely on doping concentrations. It's worth noting that leveraging the energy migration effect among lanthanide ions across multilayered structures can additionally delay UCL, leading to more pronounced phase lags even at lower modulation frequencies than analyzed here.[12]

In the context of modulated laser excitation, the average excitation intensity is an important factor. In this regard, a fixed modulation depth (M_{exc} = 1.0) and modulation frequency (f = 500 Hz) were employed to examine how the average excitation intensity influences the phase lag. As illustrated in Fig. 2f, higher average excitation intensities result in significantly smaller phase lags for the current UCNP system. On the other hand, the variation of ϕ at excitation intensities around 100 W cm^{-2} (as used in the simulations and a reasonable excitation intensity applied in UCNP-based imaging experiments) is minor. Nonetheless, to extract reliable phase lag information, this calls for some caution and control of the laser irradiance applied.

2.3 Spatial shift of the luminescence pattern of moving UCNPs under structured illumination

Using the TFD response of UCNPs presented in Fig. 2b, obtained with parameter values from Table S1 (ESI†), the spatial shift of the UCL pattern of these nanoparticles was analyzed when flowing at a uniform velocity, v, in a channel (with length L = 200 μm). At the same time, the UCNPs were subject to a stationary, structured excitation pattern:

$$I_{exc}(x) = I_{exc}\left[\frac{1+\sin(2\pi x/\Lambda)}{2}\right], \quad (5)$$

where x is the coordinate, Λ = 2 μm is the spatial period, and I_{exc} = 100 W cm^{-2} is the maximum excitation intensity.

Initially, a constant nanoparticle velocity (v_c) along the carrier flow was considered, typical for cerebral vasculature (1–10 mm s^{-1}). The time-dependent UCL intensities $I_{em}(t)$ of the moving nanoparticles generated by the structured illumination pattern $I_{exc}(x)$ were modeled using the rate equations describing UCL kinetics (see Section S1, ESI†), applying a linear conversion between space and time due to nanoparticle motion:

$$t = \frac{x}{v_c}. \quad (6)$$

Here, x denotes the nanoparticle location relative to the channel entrance, translating the structured illumination pattern $I_{exc}(x)$ into a time-domain periodic excitation function $I_{exc}(t)$. With Λ = 2 μm and a flow velocity range $v_c \in$ [1–10] mm s^{-1}, the equivalent time-domain modulation frequency ranges from 0.5–5 kHz. Coordinate-dependent UCL intensities $I_{em}(x)$ were then calculated from $I_{em}(t)$ considering the time-to-space conversion specified in eqn (6). Subsequently, $I_{em}(x)$ was compared with $I_{exc}(x)$ to evaluate the pattern shift, where we used as an evaluation parameter the distance, $\Delta x_n(x_{em,n})$, between peaks of $I_{em}(x)$ and corresponding nearest peaks of $I_{exc}(x)$, which should be readily extracted experimentally:

$$\Delta x_n(x_{em,n}) = x_{em,n} - x_{exc,n}. \quad (7)$$

Here, $x_{em,n}$ and $x_{exc,n}$ represent the positions of the nth peaks of $I_{exc}(x)$ and $I_{em}(x)$, respectively.

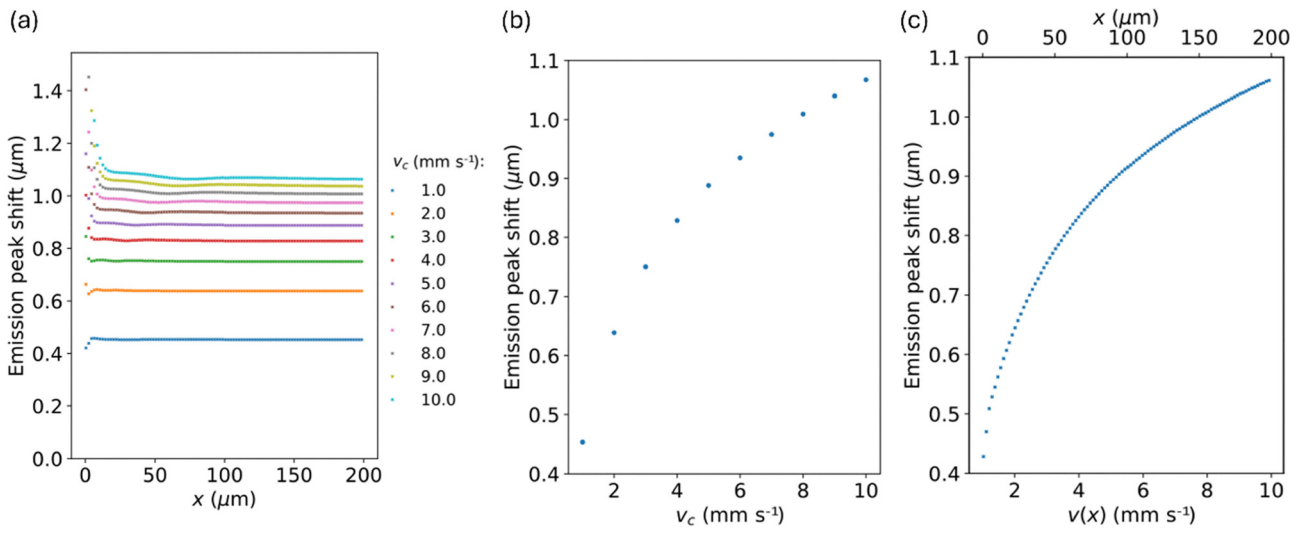

Fig. 3 (a) Spatial shift (Δx) of peaks in $I_{em}(x)$ relative to corresponding nearest peaks in the excitation pattern $I_{exc}(x)$ (eqn (7)) along a channel, when the velocity (v_c) of the nanoparticles remains constant along the channel. (b) Average spatial shift (Δx) in the channel at different v_c (constant along the channel). (c) Spatial shift (Δx) at different coordinates when the velocity is spatially varying as $v(x)$ = 0.001 + 45x [m s^{-1}] with x expressed in [m] in the equation.

Simulation results indicate that, in the very initial stage after entering the channel, there is a greater variation in the emission peak shift relative to the excitation peaks (Fig. 3a). This corresponds to the stabilization period of UCL in response to the modulated excitation (Fig. S3, ESI†), as also observed at the onset of a time-modulated excitation (Fig. S2, ESI†). However, once stabilization is established, the pattern shift Δx remains almost constant across all peaks of $I_{em}(x)$ (Fig. 3a), consistent with the constant flow velocity v_c along the channel. Hence, for simplicity, the dependence of Δx on the emission peak positions $x_{em,n}$ (eqn (7)) is disregarded in the discussion below. Importantly, Δx exhibits significant dependence on the flow velocity v_c (Fig. 3a and b). With the photophysical parameter values used for the UCNPs (Table S1, ESI†), Δx ranges from 0.45 to 1.07 μm.

It is noteworthy that such spatial shifts can be reliably determined using a wide-field optical microscope, supported by well-established computational algorithms. Resolving structured illumination patterns with spatial periods of a few micrometers is feasible with appropriate optical configurations. For instance, using a representative emission wavelength of λ = 1180 nm and an objective lens with a numerical aperture (NA) of 0.7—a value readily achievable in wide-field NIR-II imaging systems—the diffraction-limited resolution is approximately 1 μm. This resolution confirms that structured illumination patterns with a 2 μm spatial period are optically resolvable under such conditions. Additionally, subpixel interpolation techniques, which are well-established and extensively applied in PIV and PTV,[24] can further enhance the accuracy of spatial shift detections. These techniques routinely achieve localization precision in the range of 0.01 to 0.05 pixels, and similar strategies can be adapted in PP-SIV to detect small emission pattern shifts with high precision. Furthermore, the spatial period of the structured illumination pattern in PP-SIV is tunable, allowing it to be optimized based on the resolution and sampling characteristics of the optical system, while still achieving the sub-capillary spatial resolution required for cerebral vascular imaging.

Next, the complication arising from a spatially varying flow velocity was addressed. Without loss of generality, a linearly varying velocity field $v(x)$ was considered:

$$\frac{dx}{dt} = v(x) = v_0 + v_g x, \tag{8}$$

where v_0 denotes the initial velocity and v_g the velocity gradient along the x [m] direction. For a concrete example, we took v_0 = 0.001 m s^{-1} and v_g = 45 s^{-1}, yielding a velocity ranging from 1 to 10 mm s^{-1} along the channel (with the same length L = 200 μm). From the rate equations governing the UCL kinetics (Section S1, ESI†) and the time-to-space conversion given by the nanoparticle motion (eqn (8)), both the time-dependent ($I_{em}(t)$) and the coordinate-dependent ($I_{em}(x)$) UCL intensities were calculated. Subsequently, $I_{em}(x)$ and $I_{exc}(x)$ were compared and the distances between their corresponding neighboring peaks were evaluated, as described in eqn (7). As depicted in Fig. 3c, the UCL pattern does exhibit a distinct coordinate-dependent shift (Δx), affirming its dependence on the local nanoparticle velocity $v(x)$.

2.4 Retrieval of flow velocity fields

Following the distinct spatial shifts, Δx, observed for both constant and spatially varying velocities, we next shifted our focus to the inverse problem: to extract the velocity field from Δx and the recorded emission and excitation patterns. Two different approaches were considered.

The "look-up" approach. In the simplest scenario—where nanoparticles travel with constant velocity along the channel—the velocity v_c can be directly inferred from the observed peak shift Δx. To achieve this, a calibration experiment can be conducted in which known velocities (constant along the flow) are used, and the corresponding Δx values are recorded, yielding a functional relationship between Δx and v_c (Fig. 3b). For ease of interpretation, the same data as in Fig. 3b are replotted in Fig. 4a with the axes for Δx and v_c reversed. This v_c–Δx relationship, acting as prior knowledge, serves as the "look-up" curve that maps experimental measurements of Δx to estimated velocities v. Technically, Δx can be determined by identifying the peak positions of the emission profile *versus* the peaks of the excitation pattern, as described above, or by using a spatial correlation approach.

Next, the applicability of the "look-up" approach in flows with spatially varying velocities (Fig. 3c) was examined. For direct comparison, the Δx *versus* $v(x)$ data in Fig. 3c are replotted in Fig. 4a, with the axes reversed to match the format of the look-up curve. In Fig. 4a, the data points corresponding to spatially varying velocities (orange dots) show excellent agreement with the Δx- to -v_c look-up curve (blue dots from Fig. 3b), demonstrating the potential of the look-up method for velocity estimation even under non-uniform flow conditions.

For a more quantitative assessment, spline interpolation was performed on the calibration data (blue dots in Fig. 4a) to generate a continuous look-up curve for converting Δx values to flow velocities. Using this curve, the Δx values for the spatially linearly varying velocity case (Fig. 3c, or orange dots in Fig. 4a) were transformed into velocity estimates, and then compared to the actual position-dependent velocity profile defined by eqn (8), with v_0 = 0.001 m s^{-1} and v_g = 45 s^{-1}. As shown in Fig. 4b, the estimated velocities closely match the actual velocity values, with relative errors generally below 3%.

While the look-up approach is fundamentally based on the assumption that measurement conditions match those of the calibration (and is ideally suited for uniform velocity fields), these results suggest that it remains effective even under linearly varying flow conditions. Further studies are needed to assess its robustness in more complex flow environments.

The motion equation parameter-fitting approach. Unlike the empirical "look-up" method, this approach derives flow parameters by directly fitting the (measured) emission shift data to the theoretical model. Specifically, the shift in the emission profile is governed by the nanoparticle motion equation (eqn (8)) and by the nanoparticle photophysics described by rate equations (eqn (S1)–(S13), ESI†). Using this framework, we developed a parameter-fitting strategy to extract key motion

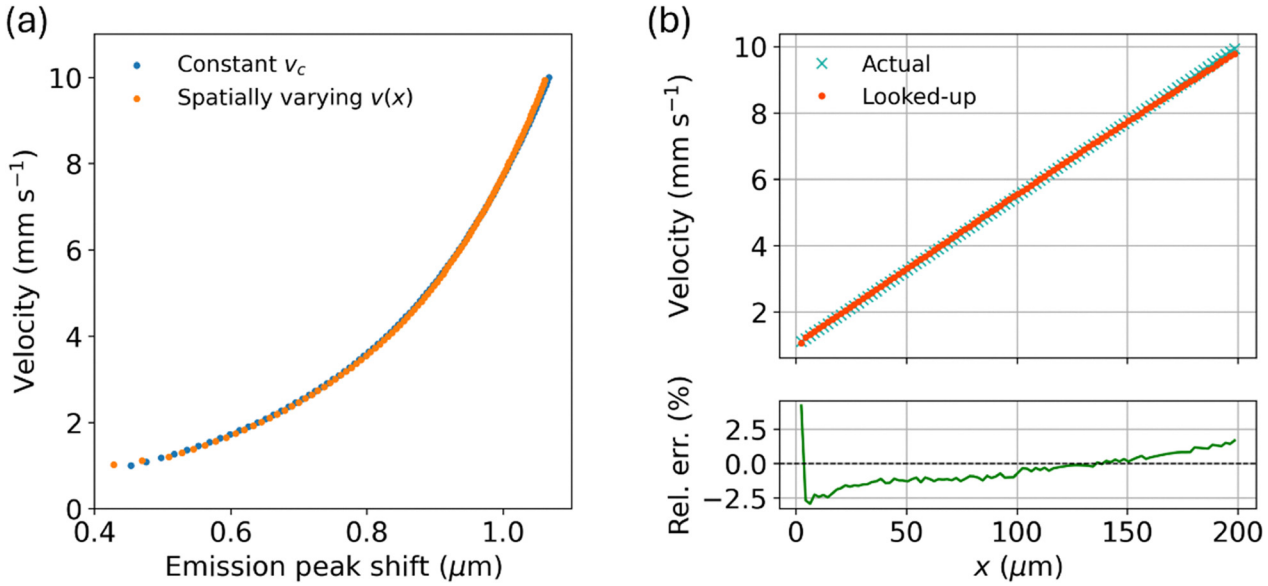

Fig. 4 "Look-up" approach for the retrieval of a flow-velocity field. (a) Blue: Δx- to -v_c look-up curve for constant flow velocities, v_c. Orange: Δx *versus* $v(x)$ data from Fig. 3c (with the flow velocity, $v(x)$, linearly increased along the channel, eqn (8)), with the axes for Δx and $v(x)$ reversed compared to Fig. 3c. (b) (upper) Retrieved flow velocities by the "look-up" method *versus* the actual flow velocity governed by eqn (8) (with v_0 = 0.001 m s^{-1} and v_g = 45 s^{-1}) and (down) the relative errors.

parameters (such as v_0 and v_g in eqn (8)) by fitting measured emission profiles to the theoretical model, based on known excitation profiles (eqn (5)) and fixed photophysical parameters (Table S1, ESI†).

For validation, the method was tested on a synthetic dataset (Fig. 5a) representing a flow with linearly increasing velocity along x, as defined by eqn (8). Random noise (up to 10%) was added to the emission profile to simulate experimental uncertainty (Fig. 5b). Using the known excitation and photophysical models as constraints, we fitted the noise-added emission data to recover the motion parameters v_0 and v_g. As shown in Fig. 5b, the fitting remained robust even with added noise, yielding accurate parameter estimates of $v_0 = (0.9995 \pm 0.0015) \times 10^{-3}$ m s^{-1} and $v_g = 44.71 \pm 0.11$ s^{-1}. The reconstructed spatial velocity profile (*via* eqn (8)) closely matched the ground-truth velocities, with relative errors generally below 1% (Fig. 5c).

Next, scenarios with more complex velocity fields were explored. For convenience, a polynomial equation was chosen, but any type of motion equation defined with explicit parameters could have been equally well used. Thus, without loss of generality, a polynomial velocity field with zero up to the third order terms was considered:

$$\frac{\mathrm{d}x}{\mathrm{d}t} = v(x) = \sum_{i=0}^{3} v_i x^i. \qquad (9)$$

As a concrete example, the parameter values in Table 1 for v_i were used, defining a velocity field shown in Fig. 5f (green). This velocity field, along with the photophysical rate equations (eqn (S1)–(S13), ESI†), was then used to calculate the emission profile, yielding the results shown in Fig. 5d. After normalizing the emission profile at its maximum and adding 10% random noise, the data was fitted to the nanoparticle motion equation (eqn (9)) to retrieve the values of the parameters v_i. The fitting successfully recovered the UCL distribution (Fig. 5e) and the actual v_i values, as listed in Table 1, resulting in a velocity field closely matching the actual velocity field (with relative errors of generally less than 3%, Fig. 5f).

This parameter-fitting approach offers a physics-informed and flexible strategy for velocity extraction, particularly well-suited for complex or nonuniform flows where empirical look-up methods may be inadequate. However, for flows with completely unknown velocity profiles, the method still requires an assumption or approximation of the underlying motion equation in order to perform the fit. In practical applications—such as velocity estimation in blood vessels—fluid dynamics modeling based on vessel geometry and flow boundary conditions may be used to inform or constrain the form of the motion equation. While the accuracy of this approach depends on the validity of the assumed motion model and the quality of the emission data, it provides a systematic pathway to analyze flows beyond the reach of direct calibration methods. Future work may explore its application to *in vivo* conditions and its performance under more complex flow conditions.

2.5 PP-SIV in 2D vasculature

This far, nanoparticles flowing in the same direction as the excitation intensity gradient of the illumination pattern (along the x direction) have been analyzed. For a flow velocity field in a 2D plane, *e.g.*, the x–y plane, spatial shift in the emission pattern in the x direction (Δx) then depends only on the component of velocity in the x direction, v_x, but is independent of any velocity component in the y direction, v_y.

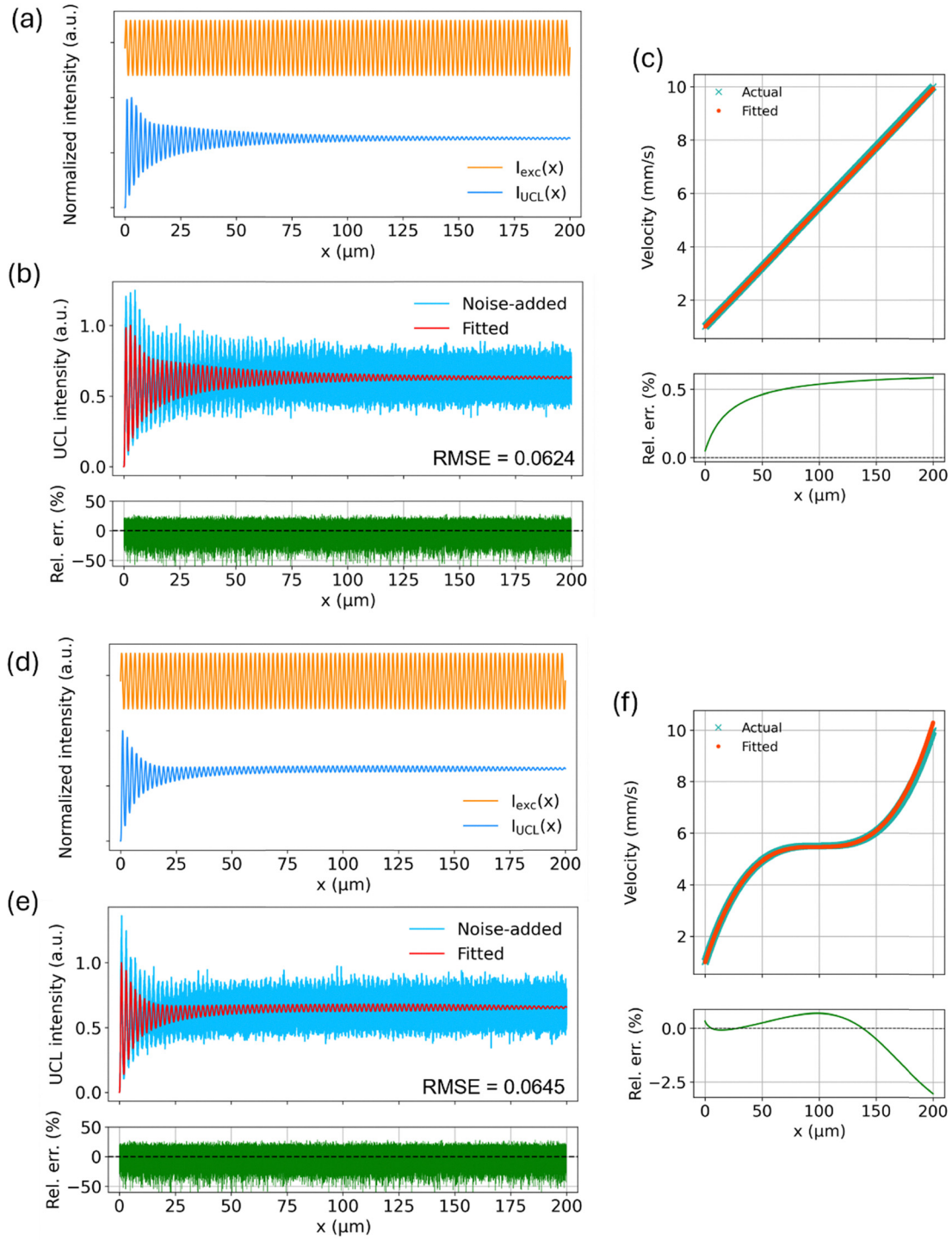

Fig. 5 The motion-equation parameter-fitting approach for the retrieval of a flow-velocity field. (a)–(c) Simulation outcomes for a linearly increasing velocity field along x, as given by eqn (8) (with v_0 = 0.001 m s^{-1} and v_g = 45 s^{-1}): (a) excitation pattern $I_{exc}(x)$ (orange, given by eqn (5)) and calculated UCL pattern $I_{em}(x)$ (blue); (b) noise-added UCL pattern and fitted UCL pattern; (c) Retrieved flow velocities by the motion-equation parameter-fitting method *versus* the actual flow velocity governed by eqn (8), with fitted parameters v_0 = (0.9995 ± 0.0015) × 10^{-3} m s^{-1} and v_g = 44.71 ± 0.11 s^{-1}. (d)–(f) Simulation outcomes as in (a)–(c), now for a velocity field varying along x, as given by eqn (9): (d) excitation pattern $I_{exc}(x)$ (orange given by eqn (5)) and calculated UCL pattern $I_{em}(x)$ (blue); (e) noise-added UCL pattern and fitted UCL pattern; (f) retrieved flow velocities by the motion-equation parameter-fitting method *versus* the actual flow velocity governed by eqn (9). RMSE: root mean square error.

To capture both velocity components in an x–y plane, v_x and v_y, the structured illumination was extended by introducing varying illumination intensities in two perpendicular dimensions. The feasibility of this approach was then explored, by considering a 2D vasculature (with its local orientation randomly generated in the x–y plane), as shown in Fig. 6a,

Table 1 Parameter values used in the simulations for Fig. 5d–f and recovered values from fitting the UCL pattern

	v_0 (m s^{-1})	v_1 (s^{-1})	v_2 (m^{-1} s^{-1})	v_3 (m^{-2} s^{-1})
Actual	1×10^{-3}	135	-1.35×10^{6}	4.5×10^{9}
Fitted (1D, Fig. 5f)	$(1.001 \pm 0.002) \times 10^{-3}$	135.7 ± 0.5	$-(1.38 \pm 0.01) \times 10^{6}$	$(4.5 \pm 0.06) \times 10^{9}$
Fitted (2D/quasi-1D, Fig. 6b)	$(1.109 \pm 0.017) \times 10^{-3}$	141.4 ± 2.7	$-(1.46 \pm 0.07) \times 10^{6}$	$(5.04 \pm 0.45) \times 10^{9}$

carrying a flow with position-dependent velocity described by:

$$\frac{ds}{dt} = v(s) = \sum_{i=0}^{3} v_i s^i, \tag{10}$$

where s is the distance along the vasculature relative to the starting position (Fig. 6b). This 2D vasculature was irradiated by a 2D pattern, with spatial periods Λ_x and Λ_y in the x and y directions, respectively,

$$I_{exc}(x,y) = I_{exc}\left[\frac{1+\sin(2\pi x/\Lambda_x)}{2}\right]\left[\frac{1+\sin(2\pi y/\Lambda_y)}{2}\right], \tag{11}$$

as depicted in Fig. 6a (gray). Similar to the 1D case, as the

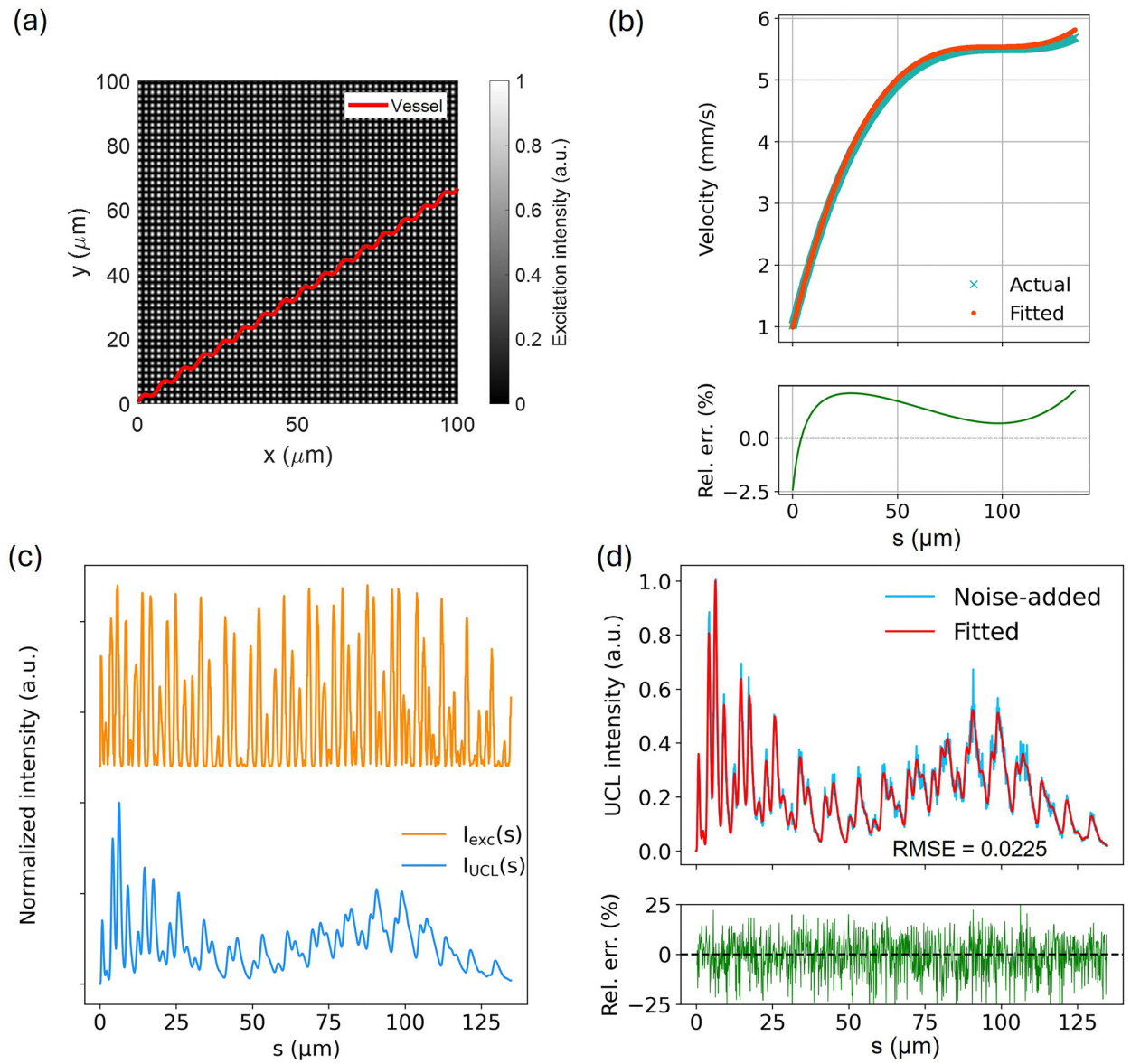

Fig. 6 The motion-equation parameter-fitting approach for the retrieval of a flow-velocity field in a 2D vasculature. (a) The 2D excitation pattern $I_{exc}(x, y)$ (gray) and the curved vessel (red) considered. (b) Flow velocities, as retrieved by the motion-equation parameter-fitting method (red) *versus* actual flow velocities (green) given by eqn (10). Bottom: Residuals between the actual and fitted velocity data. (c) Excitation ($I_{exc}(s)$, orange) and UCL ($I_{UCL}(s)$, blue) intensity profiles. (d) Fitting of noise-added UCL profile data to the theoretical model. RMSE: root mean square error.

nanoparticles move along the curved vessel, the 2D illumination pattern and the motion equation (eqn (10)) together determine the temporal excitation function that the nanoparticles are subject to along the vessel, which generates a corresponding temporal emission function, yielding a spatial emission profile.

Using a sinusoidally modulated excitation pattern in x and y (eqn (11)) with $\Lambda_x = \Lambda_y = 2$ μm, and putting the same set of v_i values as listed in Table 1 into eqn (10), the emission profile was calculated as a function of s, $I_{UCL}(s)$, using the procedure described above. Fig. 6c shows the excitation profile, $I_{exc}(s)$, as a function of s and the resulting $I_{UCL}(s)$. We then attempted to recover the flow velocity from the emission profile data. In this more complex scenario, the periodicity of the excitation profile may degrade significantly or even disappear along the vasculature, depending on its orientation on the 2D surface. This makes the phase lag dependence between the emission signal and the excitation intensity field complicated, as illustrated in Fig. 2f, which limits the applicability of the ''look-up'' approach to retrieve the flow velocity. Consequently, the motion equation parameter-fitting approach was employed, fitting the parameters v_i in the motion equation (eqn (10)) to the emission profile data. In the fitting, the nanoparticle photophysical equations (eqn (S1)–(S13), ESI†) together with the excitation profile (determined from the excitation pattern (eqn (11)) and the orientation of the vasculature on the 2D surface (Fig. 6a)) were used as prior knowledge.

In this approach, 10% random noise was again added to the calculated emission profile to generate emission profile data that resembles experimentally measured results (Fig. 6d). The subsequent fitting of the noise-added data to the theoretical model produced v_i values that closely match the actual values, as listed in Table 1. The calculated velocity field based on the retrieved v_i values successfully reproduced the actual position-dependent velocities (Fig. 6b) with a discrepancy of generally less than 3%.

3. Discussion

The PP-SIV approach is clearly distinct from previously established methods. Well-established methods such as PIV and PTV fundamentally rely on the micro-scale positioning and tracking of individual particles to assess their local displacements in order to reconstruct flow fields.[8] These approaches utilize transient luminescent or scattered signals, intentionally avoiding prolonged emissions to prevent image blurring, which negatively impacts algorithmic accuracy. Structured illumination (microscopy) has also been implemented in PIV and PTV, referred to as SIM-PIV or SIM-PTV,[25,26] but primarily as a supplementary measure to exclude signals outside the focal plane to increase resolution. Although the PP-SIV method similarly employs structured illumination, its underlying principle is fundamentally different, based on the FD response of the probes. Traditionally, FD analysis quantifies photophysical parameters (decay rates) of luminophores. In contrast, SIF leverages known photodynamics of LNPs to directly determine flow velocity. The structured illumination pattern modulates the LNP excitation spatially, thereby encoding flow velocity information within the spatial shifts of the emission pattern. In the signal source, PP-SIV exploits the inherent, long-lasting luminescence of LNPs, and analyzes an emission pattern simultaneously formed by all nanoparticles within the field of view.

The PP-SIV approach may offer distinct advantages in addressing indeterminacy issues. In the case of limited spatial resolution or reduced frame rate of the camera—where a particle may traverse more than one illumination fringe during a single exposure—the spatial shift in the emission pattern would reflect an integrated response over the illuminated flow path. This could, in principle, introduce ambiguity in determining the exact particle position or velocity if not appropriately addressed in conventionally micro-scale positioning-based methods. However, the design of the PP-SIV method inherently accounts for such scenarios through its reliance on ensemble photophysical response rather than discrete particle tracking. Our approach leverages the FD photophysical behavior of LNPs, where the observed phase shift in emission is governed by the convolution of the structured excitation pattern and the flow dynamics. Even when a particle spans multiple fringes during the integration time, the resulting FD response still encodes the net modulation experienced by the particle, and hence retains information about the average flow velocity across that path. Ultimately, while fine-grained spatial resolution is desirable, the PP-SIV framework is designed to extract flow information from collective signal behavior, making it robust to such indeterminacies.

PP-SIV is also fundamentally distinct from other imaging methods involving the integration of structured illumination microscopy (SIM) with flow or sample motion. In these techniques, the role of flow or sample motion is to facilitate or enhance SIM, rather than to directly measure flow fields. For example, in the study of Lu *et al.*,[27] sample flow was used to generate the necessary phase shifts in the illumination pattern—typically achieved *via* controlled displacement of the pattern—to enable SIM reconstruction. Similarly, in other studies,[28,29] sample motion was primarily used to encode super-resolved information across multiple raw images. These works attempted to jointly estimate both motion and the super-resolved image, primarily to correct for motion artifacts during super-resolved image reconstruction. It should also be noted that the extracted sample dynamics in such cases are typically in the micrometer-per-second (μm s^{-1}) range—significantly slower than the typical flow velocities in cerebral vasculature (1–10 mm s^{-1})—and therefore not suitable for sensing cerebral blood flow fields.

Successful implementation of PP-SIV closely relies on the luminescence kinetics of the probes. First, the kinetics need to be slow enough to allow significant spatial shifts in the emission patterns, as generated when the probes move at velocities typical for vascular blood flow within the structured illumination patterns. Based on a photophysical model and rate parameter values, either adopted or adapted from our previous work,[23] we find in our simulations that UCNPs exhibit suitable

photoluminescence kinetics in this respect. As a result, the phase lags in the TFD and SFD responses obtained fall within a useful range for PP-SIV. It should be noted that the model employed for Er^{3+}–Ho^{3+}-codoped UCNPs remains tentative, and the photophysical parameters used may not fully reflect their true values. In this work, our primary aim is not to establish a definitive upconversion mechanism or to determine the photophysical parameters with absolute accuracy. Importantly, the specific details of the model and potential variations in parameter values do not impact the overarching conclusions of our study.

A second attractive feature for PP-SIV is that the photoluminescence kinetics of UCNPs can readily be made insensitive to the local environment through nanoparticle engineering, *e.g.*, by adding thick inert shells as protection. Thereby, any effects from the local environment on the phase shifts in recorded emission patterns can be excluded, and they can be more distinctly coupled to flow velocities. Thirdly, UCNPs possess a distinct advantage given by the nonlinear dependence of their emission on the excitation intensity. On the one hand, this nonlinearity provides a basis for optical sectioning, in a similar way as in multi-photon microscopy.[10] Multiple x–y focus scans along the axial (z) direction, implementing PP-SIV at different depths, can thus open for high-quality flow imaging in 3D. Moreover, UCNPs typically possess multiple emissive states, with different nonlinear features (and photoluminescence kinetics). This opens for multiplexed PP-SIV readouts of different (spectrally separated) phase lags, offering orthogonal information about the flow velocities of the UCNPs.

Apart from UCNPs, down-conversion nanoparticles (DCNPs) also hold promise for PP-SIV, since they exhibit similar suitable luminescence kinetics. It is worth noting that Er^{3+}–Ho^{3+}-codoped UCNPs, which are the focus of our current study, may not be the most suitable candidates for implementing PP-SIV in deep tissue due to the significant water absorption near 1500 nm. However, PP-SIV is not inherently limited to any specific class of LNPs, either UCNPs or DCNPs. To mitigate the issue of water absorption, alternative NIR-II LNPs with excitation and emission profiles outside major absorption bands, can be employed to realize PP-SIV. Advances in LNP chemistry over the past decade have enabled the design of nanoparticles with tailored photophysical properties. Ho^{3+}- or Tm^{3+}-sensitized LNPs can be excited at 1143 nm and 1208/1710 nm,[30–32] respectively—wavelengths at which both water absorption and tissue scattering are significantly lower. These systems all exhibit key characteristics—such as the involvement of long-lived NIR excited states (with lifetimes up to several milliseconds) and multiple transitions and energy transfer processes—that are inherently beneficial for PP-SIV. Furthermore, through appropriate nanoparticle engineering, especially by employing core-(multi)shell structures, the luminescence kinetics of LNPs can be flexibly tuned across a broad range.[12] This tunability offers strong potential for optimizing TFD and SFD responses to better meet the requirements of PP-SIV applications.

Also, other luminophores with long luminescence lifetimes can be suitable candidates for PP-SIV. These may include phosphorescent materials with luminescence lifetimes up to milliseconds, such as carbonized polymer dots, which have been reported to have long-lived room-temperature phosphorescence (up to tens of milliseconds lifetime).[33] In addition, fluorescent proteins with slow dark-state photodynamics may serve as probes for PP-SIV, for which the fluorescently active part is hidden inside the protein so that the dark state kinetics are inert to environmental conditions.

In this study, the implementation of PP-SIV is based on analyzing the phase lag. Similar to FD lifetime measurements,[10] modulation depth (MD) could potentially serve as an additional parameter to characterize velocities by PP-SIV. However, for this readout to be useful for PP-SIV, background counts have to be to accurately accounted for in the experiments to extract true MD data. While this would require additional effort, investigating the use of MD as a parallel readout parameter to the pattern shift in PP-SIV is a promising avenue for future research.

The presented results consider velocity distributions along the flow, but are based on a uniform flow across the channels/vessels. However, we do not anticipate any fundamental obstacles by extending the PP-SIV concept to a 2D laminar flow with a non-uniform velocity distribution across the flow direction. In such case, the 2D laminar flow can be decomposed into several ''thin'' flows along the vessel, each of which can be analyzed using the approach described here. The results from all subflows can then be combined to reconstruct the entire flow velocity field. Turbulent flows in the vessels will be more difficult to quantify but may nonetheless be detected by a combination of spatial shifts, and with a loss of MD in the recorded emission patterns. In the simulated data, we have considered image recordings extending over approximately 10–100 ms. This is fast enough to capture the variation of flow speeds within heartbeat cycles of humans ($\sim$70 min^{-1}). However, also for *e.g.* mice, with approximately 10-fold higher heartbeat frequencies, this should also be possible, if necessary by triggering the image capture to different phases of the heartbeat cycle.

4. Conclusions

In this work, we present the PP-SIV concept for flow imaging, and have validated the concept through comprehensive numerical simulations, with lanthanide UCNPs as potential probe candidates. Our simulations show that UCNPs offer several attractive features for PP-SIV, including slow and tunable luminescence kinetics, well compatible with camera-based recording. Moreover, multiple emission lines with distinct lifetimes and phase lags can open for multiplexed readouts, and nonlinear responses in the emission for optical sectioning and 3D flow analyses. Apart from UCNPs, also other emitters are likely feasible for PP-SIV, as discussed above.

By implementing PP-SIV, the velocity distribution along the flow at a given depth can be extracted from a single emission pattern measurement, using the applied excitation pattern as reference. This approach eliminates the need for source scans, which currently pose a major limitation to the imaging speed of state-of-the-art blood flow imaging techniques, even in 2D. The time saved by scanning-free surface imaging in PP-SIV could

instead be allocated to multiple focal plane recordings along the beam axial direction, enabling 3D flow imaging with sufficient speed for real-time monitoring of most hemodynamic events. Taken together, our study presents the potential of PP-SIV for flow imaging and provides a solid basis for further experimental validations.

4.1 Methods

All the forward simulations and inverse problems were addressed by performing time-course or parameter estimation tasks in the open-source software COPASI through its python interface BasiCO.[34,35] In the forward calculations of time-resolved upconversion luminescence intensities, the nanoparticle photophysics equations (eqn (S1)–(S13) in the ESI†) were used as the forward model with the time-dependent excitation intensity as the input. In the calculations of the spatial upconversion luminescence intensity patterns, the nanoparticle photophysics equations (eqn (S1)–(S13) in the ESI†) and the excitation intensity spatial profile (eqn (5) and (11)) coupled with the motion equation (eqn (6) and (8)–(10)) were used. To solve the inverse problems, the nanoparticle photophysics equations (eqn (S1)–(S13) in the ESI†) and the excitation intensity spatial profile (eqn (5) or (11)) were used as prior knowledge, and the upconversion luminescence intensity data were fitted to the motion equation to retrieve the flow velocity parameters.

Author contributions

Haichun Liu – conceptualization, methodology, investigation, data curation, formal analysis, funding acquisition, project administration, software, resources, validation, visualization, writing – original draft. Jerker Widengren – conceptualization, formal analysis, funding acquisition, project administration, resources, writing – review & editing.

Conflicts of interest

There are no conflicts of interest to declare.

Data availability

The code used for data analysis during this study is available upon reasonable request from the corresponding authors.

Acknowledgements

H. L. and J. W. acknowledge financial support from the ÅForsk Foundation (23-322) and the Swedish Foundation for Strategic Research (SSF, BENVAC RMX18-0041).

References

1 B. M. Ances, J. H. Greenberg and J. A. Detre, Laser Doppler Imaging of Activation-Flow Coupling in the Rat Somatosensory Cortex, *NeuroImage*, 1999, **10**, 716–723, DOI: 10.1006/nimg.1999.0510.

2 S. Ogawa, *et al.*, Intrinsic signal changes accompanying sensory stimulation: functional brain mapping with magnetic resonance imaging, *Proc. Natl. Acad. Sci. U. S. A.*, 1992, **89**, 5951–5955, DOI: 10.1073/pnas.89.13.5951.

3 D. Kleinfeld, P. P. Mitra, F. Helmchen and W. Denk, Fluctuations and stimulus-induced changes in blood flow observed in individual capillaries in layers 2 through 4 of rat neocortex, *Proc. Natl. Acad. Sci. U. S. A.*, 1998, **95**, 15741–15746, DOI: 10.1073/pnas.95.26.15741.

4 A. Y. Shih, *et al.*, Two-photon microscopy as a tool to study blood flow and neurovascular coupling in the rodent brain, *J. Cereb. Blood Flow Metab.*, 2012, **32**, 1277–1309, DOI: 10.1038/jcbfm.2011.196.

5 E. Chaigneau, M. Roche and S. Charpak, Unbiased Analysis Method for Measurement of Red Blood Cell Size and Velocity With Laser Scanning Microscopy, *Front. Neurosci.*, 2019, **13**, 644, DOI: 10.3389/fnins.2019.00644.

6 K. Kisler, *et al.*, In vivo imaging and analysis of cerebrovascular hemodynamic responses and tissue oxygenation in the mouse brain, *Nat. Protoc.*, 2018, **13**, 1377–1402, DOI: 10.1038/nprot.2018.034.

7 J. L. Fan, *et al.*, High-speed volumetric two-photon fluorescence imaging of neurovascular dynamics, *Nat. Commun.*, 2020, **11**, 6020, DOI: 10.1038/s41467-020-19851-1.

8 H. Wang, L. Hong and L. P. Chamorro, Micro-Scale Particle Tracking: From Conventional to Data-Driven Methods, *Micromachines*, 2024, **15**, 629, DOI: 10.3390/mi15050629.

9 L. Liu, *et al.*, Er^{3+}-Sensitized 1530 nm to 1180 nm Second Near-Infrared Window Upconversion Nanocrystals for In Vivo Biosensing, *Angew. Chem., Int. Ed.*, 2018, **57**, 7518–7522, DOI: 10.1002/anie.201802889.

10 J. R. Lakowicz in *Principles of Fluorescence Spectroscopy*, ed. J. R. Lakowicz, Springer US, 3rd edn, 2006, pp. 157–204.

11 A. Chmyrov, T. Sandén and J. Widengren, Recovery of Photoinduced Reversible Dark States Utilized for Molecular Diffusion Measurements, *Anal. Chem.*, 2010, **82**, 9998–10005, DOI: 10.1021/ac1014047.

12 H. Liu, *et al.*, Phase angle encoded upconversion luminescent nanocrystals for multiplexing applications, *Nanoscale*, 2017, **9**, 1676–1686, DOI: 10.1039/c6nr09349c.

13 L. Labrador-Páez, *et al.*, Frequency-Domain Method for Characterization of Upconversion Luminescence Kinetics, *J. Phys. Chem. Lett.*, 2023, **14**, 3436–3444, DOI: 10.1021/acs.jpclett.3c00269.

14 C. Sun, *et al.*, J-Aggregates of Cyanine Dye for NIR-II in Vivo Dynamic Vascular Imaging beyond 1500 nm, *J. Am. Chem. Soc.*, 2019, **141**, 19221–19225, DOI: 10.1021/jacs.9b10043.

15 G. Hong, *et al.*, Through-skull fluorescence imaging of the brain in a new near-infrared window, *Nat. Photonics*, 2014, **8**, 723–730, DOI: 10.1038/nphoton.2014.166.

16 Y. Zhang, *et al.*, Ag_2S Quantum Dot: A Bright and Biocompatible Fluorescent Nanoprobe in the Second Near-Infrared Window, *ACS Nano*, 2012, **6**, 3695–3702, DOI: 10.1021/nn301218z.

17 Y. Zhang, *et al.*, Biodistribution, pharmacokinetics and toxicology of Ag_2S near-infrared quantum dots in mice,

Biomaterials, 2013, **34**, 3639–3646, DOI: **10.1016/j.biomaterials.2013.01.089**.

18 Y. Zhong, *et al.*, Boosting the down-shifting luminescence of rare-earth nanocrystals for biological imaging beyond 1500 nm, *Nat. Commun.*, 2017, **8**, 737, DOI: **10.1038/s41467-017-00917-6**.

19 Y. Zhong, *et al.*, In vivo molecular imaging for immunotherapy using ultra-bright near-infrared-IIb rare-earth nanoparticles, *Nat. Biotechnol.*, 2019, **37**, 1322–1331, DOI: **10.1038/s41587-019-0262-4**.

20 F. Ren, *et al.*, Shortwave-infrared-light-emitting probes for the in vivo tracking of cancer vaccines and the elicited immune responses, *Nat. Biomed. Eng.*, 2023, **8**, 726–739, DOI: **10.1038/s41551-023-01083-5**.

21 F. Wang, Y. Zhong, O. Bruns, Y. Liang and H. Dai, In vivo NIR-II fluorescence imaging for biology and medicine, *Nat. Photonics*, 2024, **18**, 535–547, DOI: **10.1038/s41566-024-01391-5**.

22 Z. Fang, *et al.*, Oxyhaemoglobin saturation NIR-IIb imaging for assessing cancer metabolism and predicting the response to immunotherapy, *Nat. Nano*, 2024, **19**, 124–130, DOI: **10.1038/s41565-023-01501-4**.

23 X. Guo, *et al.*, Achieving low-power single-wavelength-pair nanoscopy with NIR-II continuous-wave laser for multichromatic probes, *Nat. Commun.*, 2022, **13**, 2843, DOI: **10.1038/s41467-022-30114-z**.

24 A. Mohammed Raad, *et al.*, A Review in Particle Image Velocimetry Techniques (Developments and Applications), *J. Adv. Res. Fluid Mech. Thermal Sci.*, 2024, **65**, 213–229.

25 M. Spadaro and M. Yoda, Structured illumination microscopy: a new way to improve the axial spatial resolution of microscale particle velocimetry, *Exp. Fluids*, 2020, **61**, 127, DOI: **10.1007/s00348-020-02965-z**.

26 M. Spadaro and M. Yoda, Resolution considerations for structured illumination microscale particle tracking velocimetry, *Exp. Fluids*, 2023, **64**, 33, DOI: **10.1007/s00348-022-03563-x**.

27 C.-H. Lu, N. C. Pégard and J. W. Fleischer, Flow-based structured illumination, *Appl. Phys. Lett.*, 2013, **102**, 161115, DOI: **10.1063/1.4802091**.

28 R. Cao, F. L. Liu, L.-H. Yeh and L. Waller, Dynamic Structured Illumination Microscopy with a Neural Space-time Model, in *2022*, *IEEE Int. Conf. Computational Photography*, 2022, **(ICCP)**, 1–12.

29 R. Cao, N. S. Divekar, J. K. Nunez, S. Upadhyayula and L. Waller, Neural space-time model for dynamic multi-shot imaging, *Nat. Methods*, 2024, **21**, 2336–2341, DOI: **10.1038/s41592-024-02417-0**.

30 X. Wang, *et al.*, An Emerging Toolkit of Ho^{3+} Sensitized Lanthanide Nanocrystals with NIR-II Excitation and Emission for in Vivo Bioimaging, *J. Am. Chem. Soc.*, 2025, **147**, 2182–2192, DOI: **10.1021/jacs.4c16451**.

31 H. Zhang, *et al.*, Tm^{3+}-Sensitized NIR-II Fluorescent Nanocrystals for In Vivo Information Storage and Decoding, *Angew. Chem., Int. Ed.*, 2019, **58**, 10153–10157, DOI: **10.1002/anie.201903536**.

32 Z.-H. Chen, *et al.*, NIR-II Anti-Stokes Luminescence Nanocrystals with 1710 nm Excitation for in vivo Bioimaging, *Angew. Chem., Int. Ed.*, 2025, **64**, e202416893, DOI: **10.1002/anie.202416893**.

33 C. Zheng, S. Tao, X. Zhao, C. Kang and B. Yang, Crosslink-Enhanced Emission-Dominated Design Strategy for Constructing Self-Protective Carbonized Polymer Dots With Near-Infrared Room-Temperature Phosphorescence, *Angew. Chem., Int. Ed.*, 2024, **63**, e202408516, DOI: **10.1002/anie.202408516**.

34 S. Hoops, *et al.*, COPASI–a COmplex PAthway SImulator, *Bioinformatics*, 2006, **22**, 3067–3074, DOI: **10.1093/bioinformatics/btl485**.

35 F. T. Bergmann, BASICO: A simplified Python interface to COPASI, *J. Open Source Softw.*, 2023, **8**(90), 5553, DOI: **10.21105/joss.05553**.